The Astrophysical Journal Letters, 931:L32 (8pp), 2022 June 1 https://doi.org/10.3847/2041-8213/ac715a

Current-sheet Oscillations Caused by the Kelvin–Helmholtz Instability at the Loop Top of Solar Flares

Yulei Wang[1,2], Xin Cheng[1,2,3], Zining Ren[1,2], and Mingde Ding[1,2]
[1] School of Astronomy and Space Science, Nanjing University, Nanjing 210023, People's Republic of China; xincheng@nju.edu.cn
[2] Key Laboratory for Modern Astronomy and Astrophysics, Nanjing University, Ministry of Education, Nanjing 210023, People's Republic of China
[3] Max Planck Institute for Solar System Research, Gottingen, D-37077, Germany
Received 2022 April 7; revised 2022 May 9; accepted 2022 May 19; published 2022 June 6

Abstract

Current sheets (CSs), long stretching structures of magnetic reconnection above solar flare loops, are usually observed to oscillate; their origins, however, are still puzzled at present. Based on a high-resolution 2.5D MHD simulation of magnetic reconnection, we explore the formation mechanism of CS oscillations. We find that large-amplitude transverse waves are excited by the Kelvin–Helmholtz instability at the highly turbulent cusp-shaped region. The perturbations propagate upward along the CS with a phase speed close to local Alfvén speed thus resulting in the CS oscillations we observe. Though the perturbations damp after propagating for a long distance, the CS oscillations are still detectable. In terms of detected CS oscillations, with a combination of differential emission measure techniques, we propose a new method for measuring the magnetic field strength of the CS and its distribution in height.

Unified Astronomy Thesaurus concepts: Solar flares (1496); Solar magnetic reconnection (1504); Magnetohydrodynamical simulations (1966)

Supporting material: animations

1. Introduction

Solar flares are one of the most energetic phenomena in the solar atmosphere and often appear as a sudden emission enhancement over the whole electromagnetic spectrum. In the past decades, their energy release mechanism, spatial structures, and dynamical properties have been widely studied. The well-known standard flare model summarizes several key features of flares, including two parallel bright ribbons, a cusp-shaped loop-top structure, an elongated current sheet (CS), and the erupting magnetized plasmoid (CSHKP; Carmichael 1964; Sturrock 1966; Hirayama 1974; Kopp & Pneuman 1976; Shibata et al. 1995; Lin & Forbes 2000). These features are all closely related to the fundamental energy release process, i.e., magnetic reconnection.

Above the flare loops, the thin and long stretching, or ray-like high-temperature structures, typically of 10–20 million K, are suggestive of model-predicted CSs (see Ciaravella et al. 2002; Ko et al. 2003; Webb et al. 2003; Liu et al. 2010; Patsourakos & Vourlidas 2011). For a few events, it is observed that the thin and long CSs even extend to the high corona for several solar radii and connect to the erupting coronal mass ejections (CMEs; e.g., Cheng et al. 2018). Because of the large Lundquist number of the corona, plenty of small-scale plasmoid structures are generated by tearing-mode instability and then propagate upward and downward along the CSs (e.g., Shen et al. 2011; Mei et al. 2012; Lin et al. 2015; Lee et al. 2021).

Interestingly, CSs usually also present a transverse oscillation. Chen et al. (2010) reported propagating large-scale waves along a helmet streamer CS with a period of 1 hr and wavelength of several solar radii. Similar waves with a shorter period of 30 minutes were also captured by Ling et al. (2014). Samanta et al. (2019) analyzed a similar but more slowly propagating wave ($\sim$19 km s^{-1}) along the ray-like CSs and proposed that they might be vortex shedding in the corona. Verwichte et al. (2005) found that the supra-arcade downflows, probably corresponding to the reconnection outflows, as well as the bright CS-like supra-arcade fans, also oscillated but the periods were usually much shorter, mostly <5 minutes. The first evidence for CS oscillations was reported by Li et al. (2016), who found that they had a period of $\sim$11 minutes and propagated away from the Sun with a speed of $\sim$200 km s^{-1}. Figure 1 exhibits a similar CS oscillation event captured by the Atmospheric Imaging Assembly (AIA) on board the Solar Dynamic Observatory (Lemen et al. 2012; Pesnell et al. 2012) on 2011 October 22. One can clearly see that the ray-like structures above the flare loops, supposed to be the CSs, sway in the plane of the sky.

CS oscillations might be related to the fine processes at the cusp-shaped flare loop region where turbulent flows and plenty of shocks take place (see McKenzie 2013; Takasao et al. 2015; Shen et al. 2018; Cai et al. 2019; Ye et al. 2020). Takahashi et al. (2017) reported that, under high-Lundquist-number conditions, the quasiperiodic oscillations were driven by the horizontal motions of termination shocks (TSs) with oblique fronts at the flare loop top and the buffer region at the CME bottom. Recently, Xie et al. (2021) performed a similar simulation and found that the oscillations are caused by the Rayleigh–Taylor instability (RTI) in the buffer region with the break of symmetry and that the oscillations propagated toward the Sun and caused prominent displacements of the CS structure.

In this letter, we further explore the origins of CS oscillations based on a high-resolution 2.5D magnetic reconnection model. We found that the Kelvin–Helmholtz instability (KHI) of the

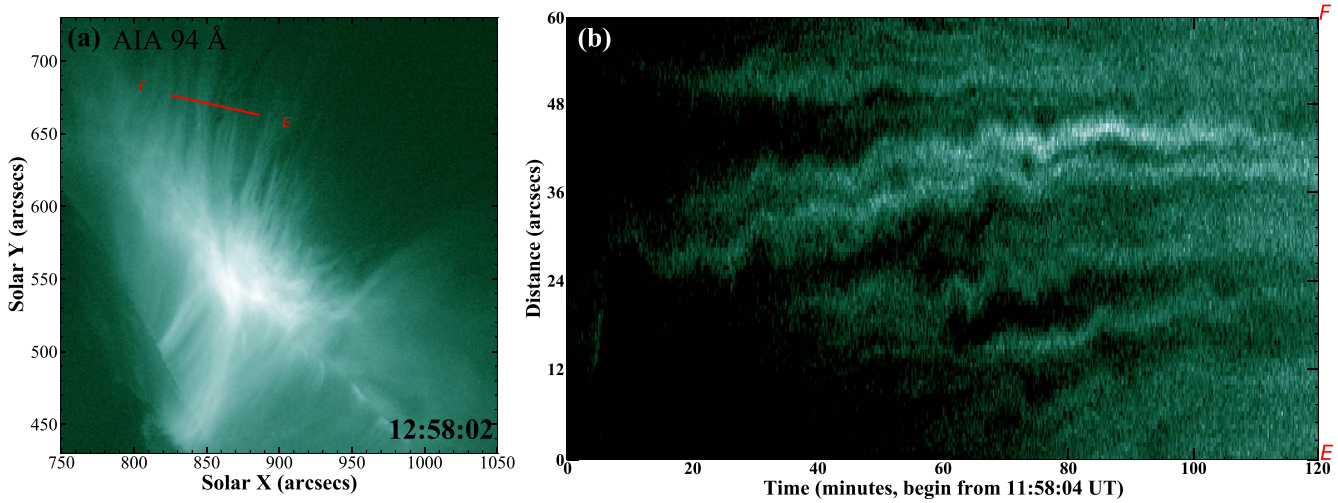

Figure 1. A loop-top CS oscillation event. (a) AIA 94 Å image showing the ray-like structures above the flare loops recorded on 2011 October 22 12:58:02 UT suggestive of the elongated CSs (see also Webb et al. 2003; Li et al. 2016). (b) Slice-time plot showing the oscillations of the ray-like CSs. The location of the slice Front-End (FE) is indicated in panel (a). An animation of this figure is available online. The video, with a duration of 15 s, shows the evolution of the ray-like structures in the 94 Å passband from 11:58:04 to 13:57:04 on 2011 October 22.

(An animation of this figure is available.)

TS tail flow initializes the development of asymmetry flows and thus gives rise to CS oscillations. Furthermore, we analyze the propagation properties of perturbations causing CS oscillations and confirm the method we propose for estimating the magnetic field strength of the CS and its distribution in height. Section 2 briefly introduces our numerical model. The main results are presented in Section 3, which are followed by a summary and discussion.

2. Numerical Model

Our numerical model is based on the resistive MHD equations including gravity, anisotropic thermal condition, radiation cooling, and background heating:

$$\begin{aligned}
&\frac{\partial \rho}{\partial t} + \nabla \cdot (\rho \boldsymbol{u}) = 0,\\
&\frac{\partial (\rho \boldsymbol{u})}{\partial t} + \nabla \cdot (\rho \boldsymbol{u}\boldsymbol{u} - \Gamma \boldsymbol{\Gamma} + P^{*}\boldsymbol{I}) = \rho \boldsymbol{g},\\
&\frac{\partial e}{\partial t} + \nabla \cdot [(e + P^{*})\boldsymbol{u} - \boldsymbol{B}(\boldsymbol{B} \cdot \boldsymbol{u})]\\
&= \rho \boldsymbol{g} \cdot \boldsymbol{u} + \nabla \cdot (\kappa_{\parallel} \hat{\boldsymbol{b}}\hat{\boldsymbol{b}} \cdot \nabla T) - n_i n_e \Lambda(T) + H,\\
&\frac{\partial \boldsymbol{B}}{\partial t} - \nabla \times (\boldsymbol{u} \times \boldsymbol{B}) = -\nabla \times (\eta \boldsymbol{J}),\\
&\boldsymbol{J} = \nabla \times \boldsymbol{B}, \qquad (1)
\end{aligned}$$

where, $P^{*} = p + B^2/2$, $e = p/(\gamma - 1) + \rho u^2/2 + B^2/2$, $\gamma = 5/3$, n_e, and n_i are, respectively, the number density of electrons and ions, and other variables are denoted by standard notations. The conductivity parallel with magnetic field is determined by $\kappa_{\parallel} = \kappa_0 T^{2.5}$, where $\kappa_0 = 6.67 \times 10^5$ erg s^{-1} cm^{-1} K$^{-3.5}$. The gravity acceleration is calculated by $\boldsymbol{g} = -g\hat{\boldsymbol{e}}_y$, where $g = g_0/(1 + y/R_{\odot})^2$, $R_{\odot}$ denotes the solar radii, and $g_0 = 2.7390 \times 10^4$ cms^{-2}. We use a widely used optically thin radiation cooling function $\Lambda(T)$ (see Klimchuk et al. 2008; Ye et al. 2020; Shen et al. 2022). The background heating, $H = n_i n_e \Lambda(T_{\rm cor})$, is supposed to maintain the initial energy balance in the corona and also keep balancing the cooling effect in the bottom chromosphere region ($y < 0.2$), where $T_{\rm cor}$ is the initial coronal temperature. In this letter, all variables are normalized according to constant units identical to Wang et al. (2021). Physical units of main variables are listed in Table 1.

Table 1
Physical Units of Main Variables

Units	Symbols	Values
Space	L_0	50 Mm
Mass Density	ρ_0	1.67×10^{-14} g cm^{-3}
Magnetic Strength	B_0	20 G
Time	t_0	114.61 s
Velocity	u_0	436 km s^{-1}
Temperature	T_0	11.52 MK

The initial temperature of the gravitationally stratified atmosphere is set as

$$T(y) = \frac{T_{\rm cor} - T_{\rm chr}}{2} \tanh\left(\frac{y - h_{\rm chr}}{w_{\rm tr}}\right) + \frac{T_{\rm cor} + T_{\rm chr}}{2}, \qquad (2)$$

where, $T_{\rm cor} = 0.1$, $T_{\rm chr} = 0.002$, $h_{\rm chr} = 0.12$, and $w_{\rm tr} = 0.02$. The initial pressure profile, calculated by $p(y) = p_0 \exp\left(-\int_0^y g/T \mathrm{d}y'\right)$, is set to balance gravity (see also Ye et al. 2020), where $p_0 = p_{\rm ref} \exp\left(\int_0^{y_{\rm ref}} g/T \mathrm{d}y'\right)$ and $p_{\rm ref} = 0.08$ is the pressure at $y_r = 0.22$. The initial force-free magnetic field, identical to Wang et al. (2021), forms a vertical CS resembling that in the CSHKP model. To trigger the reconnection, we use a localized anomalous resistivity near $y = 0.5$ and $x = 0$, which is also identical to Wang et al. (2021). The initial velocity is set to zero everywhere. The initial static equilibrium of the atmosphere is exactly satisfied in the corona region ($y > 0.2$), but is slightly perturbed in the transition region ($0.1 < y < 0.2$) where the thermal conduction term causes a localized downward energy flow due to the temperature gradient. However, this initial perturbation in the

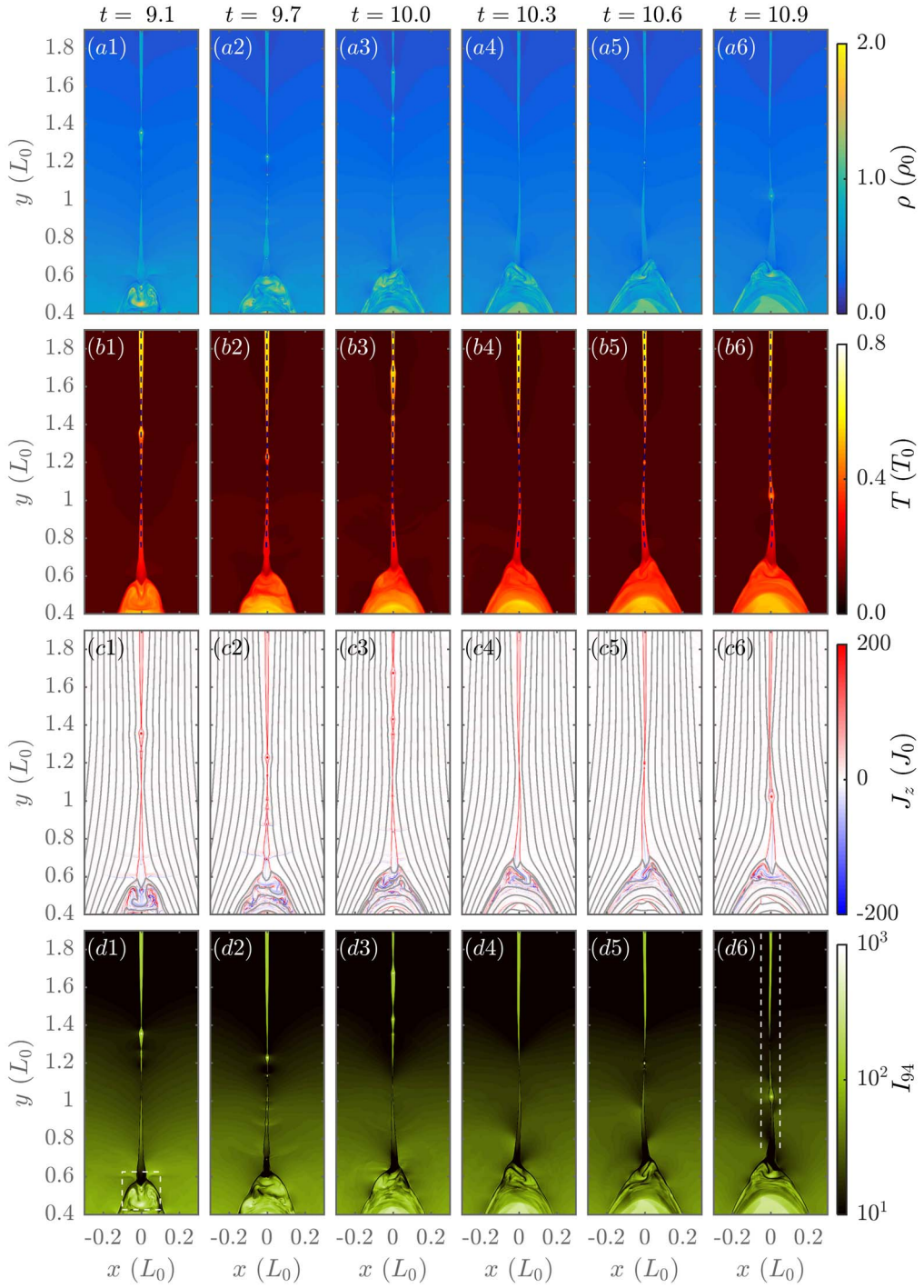

Figure 2. Distributions of density ρ, temperature T, current density J_z, and synthetic AIA 94 Å images at six moments. The region is selected to emphasize the loop-top region and the CS. The blue dashed curves in the temperature profile (second row) are the middle of the CS. The gray curves in panels (c1)–(c6) exhibit the magnetic field lines. The dashed box in panel (d1) marks the region as shown in Figure 3. The dashed lines in panel (d6) show the CS outer boundary used in Figure 5. The unit of the intensity for the 94 Å images is DN pixel^{-1} s^{-1}. An animation of this figure is available online. The video, with a duration of 24 s, shows the evolutions of ρ, T, J_z, and synthetic AIA 94 Å image in $t \in [0, 12]$.

(An animation of this figure is available.)

transition region is ignorable compared with the dominating reconnection process (see the animation of Figure 2). The boundary conditions are arranged as follows. The left ($x = -0.5$) and right ($x = 0.5$) are free boundaries, the top ($y = 2$) is a no-inflow boundary, and the bottom ($y = 0$) is a symmetric boundary.

The above system is simulated with the Athena++ code (Stone et al. 2020). We use the HLLD Riemann solver (Miyoshi & Kusano 2005), the two-order piecewise linear method, and the two-order van Leer predictor-corrector scheme to solve the conservation part of Equation (1). The resistivity, thermal conduction, gravity, radiation cooling, and heating

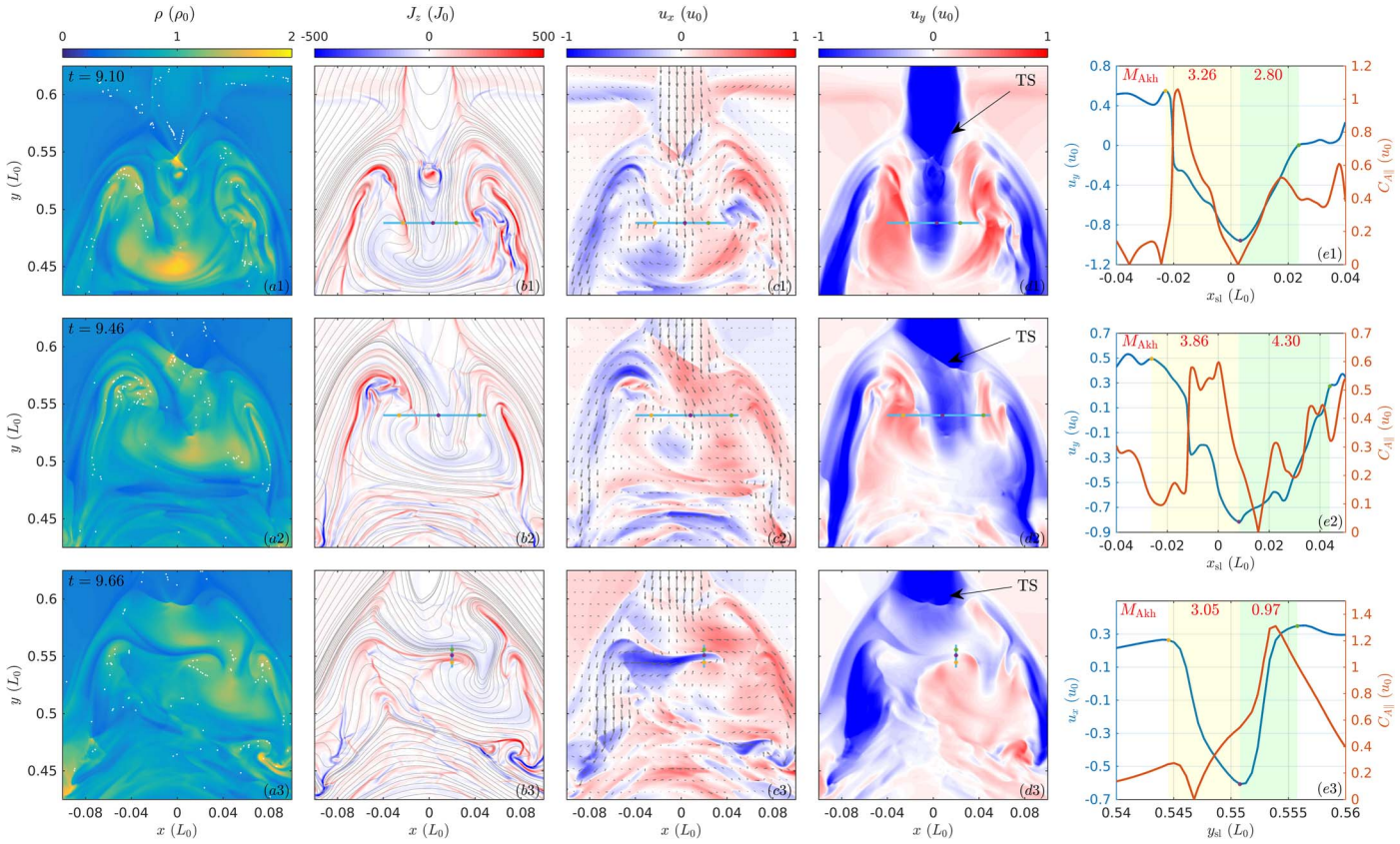

Figure 3. (a1)–(d1) Distributions of ρ, J_z, u_x, and u_y, where the blue line segments are approximately perpendicular to the shear layers. (e1) The sheared velocity (blue curves) and $C_{A\|}$ (orange curve) along the line segments. The positions of local velocity extreme values are marked by the orange, purple, and green dots, which are also used to define the ranges of shear layers as highlighted by the yellow and green shades in panel (e1). The values of $M_{\rm Akh}$ are shown in red at the top of the panel. The gray curves in panel (b1) denote the magnetic field lines, while the arrows in panel (c1) exhibit the velocity field. The white dots in panel (a1) mark the positions of $\lambda_c < 0.1$, namely, where the RTI can potentially be triggered. (a2)–(e2) and (a3)–(e3) are the same as (a1)–(e1) but for different moments. An animation of this figure is available online. The video, with a duration of 15 s, shows the evolutions of ρ, J_z, u_x, and u_y at the loop-top region in $t \in [9, 10.5]$. The positions of $\lambda_c < 0.1$ are also marked in the movie of ρ.

(An animation of this figure is available.)

terms are calculated by the explicit operator splitting method. The two-order RKL2 super-time-stepping algorithm is adopted to reduce computational costs (Meyer et al. 2014). Uniform Cartesian grids are used in both directions, namely, 1920 and 3840 grids in x and y directions, respectively. The pixel scale is $\Delta L = \Delta x = \Delta y = 26$ km. The maximum simulation time in our simulation is $t_{\rm max} = 12$, which corresponds to 23 minutes in physical time.

3. Results

3.1. Overview

The magnetic reconnection is initiated at a small region that has an anomalous resistivity. At $t = 5$, a flare loop system and an erupting plasmoid above the principal X-point appear (see also Yokoyama & Shibata 2001; Takasao et al. 2015). Under the small background resistivity, plasmoid instability dominates the reconnection and the CS is fragmented into various magnetic islands of different scales (see also Bhattacharjee et al. 2009; Shen et al. 2011; Mei et al. 2012; Ni et al. 2016; Ye et al. 2019; Kong et al. 2020; Zhao & Keppens 2020). The reconnection also shows a quasiperiodic characteristic. At $t = 7.5$, a relatively large magnetic island forms in the CS, it then moves downward and collides with the flare loop top (see the animation of Figure 2). As the island annihilates there gradually, the kinetic and magnetic energies are further released (see Wang et al. 2021). At the same time, the cusp-shaped loop top becomes highly turbulent. Following this big island, several relatively small islands are generated and also enter the loop-top region. After $t = 9$, large-size islands are rarely generated and the oscillations of the CS gradually appear. At $t = 9.1$, under the TS, the y-asymmetry of the flows starts to grow (see the first column of Figure 2). The tip of the cusp-shaped loop top show prominent oscillation after $t = 9.7$ (see Figure 2). The CS bottom sways back and forth, and the transverse waves are excited and propagate upward at the same time. To compare with the observations, following the method used by Xie et al. (2019) and Ye et al. (2020), we synthesize the AIA 94 Å images by $I_{94} = \int n_e^2 f(T) {\rm d}l = n_e^2 f(T) L_{\rm los}$, where $f(T)$ is the temperature response function, and $L_{\rm los} = 10^9$ cm is the scale of the line of sight in the z-direction. The wavelike swinging of the CS can be clearly observed in the synthesized AIA 94 Å images (see Figures 2(d1)–(d6)).

3.2. Initialization of CS Oscillations

Figure 3 exhibits the initialization phase of the CS swing at the cusp-shaped loop top. Before $t = 9.1$, the loop top is collided consecutively by bullet-like magnetic islands. Though many small-scale vortexes emerge, the loop top is approximately symmetric in the y-direction and no global horizontal

displacement is observed (see the animation of Figure 3). At $t = 9.1$, under the TS front (the downstream region), the downflow speed is still strong (see Figures 3(d1) and (e1)). Once the tail flow is blocked by the relatively stable flare loops, two backflows form on both sides (e.g., Figures 3(c1) and (d1), also see Takasao & Shibata 2016). Consequently, two shear layers form below the TS, where the KHI is triggered.

Theoretically, if the magnetic field is strong enough, the magnetic tension along the shear layer can stabilize the perturbations and thus suppress the KHI (Jones et al. 1997). The key criterion of the KHI in magnetized plasmas is the local Alfvénic Mach number of the velocity transition in shear layers (e.g., Ryu et al. 2000), which is defined as $M_{\rm Akh} = U_0/C_{A\parallel}$, where U_0 is the shear velocity, $C_{A\parallel} = B_\parallel/\sqrt{\rho}$ is the projected Alfvén speed, and $B_\parallel$ is the magnetic strength along the shear layer. To be specific, the KHI is stabilized by the magnetic tension for $M_{\rm Akh} < 2$, and if $M_{\rm Akh} > 4$, the magnetic field is too weak and the evolution of the KHI is almost fully hydrodynamical (see Ryu et al. 2000).

To estimate $M_{\rm Akh}$ of two shear layers, we set a slit perpendicular to the shear layers (see Figures 3(b1)–(d1)) and extract the profiles of the parallel velocity (here u_y) and $C_{A\parallel}$ along the slit (Figure 3(e1)). U_0 is the difference between the speeds of sheared flows (e.g., the velocity difference between the orange and purple dots in Figure 3(e1)). Because $C_{A\parallel}$ varies along the slit, the average value across the shear layers is used when calculating $M_{\rm Akh}$. As shown by Figure 3(e1), the values of $M_{\rm Akh}$ on the two shear layers (left and right) are 3.26 and 2.80, respectively, which means that the two layers are both unstable to the KHI and their evolutions are not symmetric about y-axis at $t = 9.1$. Subsequently, the plasma under the TS starts to stir significantly and the flows show different behaviors on both sides of the y-axis. At $t = 9.46$, the previously y-symmetric TS front becomes oblique (see Figure 3(d2)). Both shear layers are still unstable to the KHI (see Figure 3(e2)). The left one starts to rotate after this moment, and, at $t = 9.66$, it evolves into a horizontal layer that still satisfies the condition of the KHI (see Figures 3(c3)–(e3)). Thereafter, similar behaviors of shear layers are observed and the oscillation amplitude of the CS bottom also grows.

We now examine the condition of the RTI in the loop-top region. The RTI can be switched on if the perturbation wave along the density interface satisfies (Hillier 2016; Carlyle & Hillier 2017; Xie et al. 2021)

$$\omega^2 = -kg_\perp \frac{\rho_u - \rho_l}{\rho_u + \rho_l} + \frac{2k^2 B_\parallel^2}{\rho_u + \rho_l} < 0, \tag{3}$$

where k and ω denote, respectively, the wavenumber and frequency of the perturbation, $g_\perp$ is the acceleration of gravity perpendicular to the interface, $B_\parallel$ is the magnetic field strength parallel with the interface, and ρ_u and ρ_l are the upper and lower density, respectively. Equation (3) means that the perturbation wavelength $\lambda = 2\pi/k$ should be larger than the critical length $\lambda_c = 4\pi B_\parallel^2/g_\perp(\rho_u - \rho_l)$ for the sake of initiating the RTI. The density interface where the RTI might grow satisfies $\hat{\boldsymbol{e}}_y \cdot \nabla\rho > 0$ to guarantee $\rho_u - \rho_l > 0$ and its normal vector is $\hat{\boldsymbol{n}}_{\rm rt} = \nabla\rho/|\nabla\rho|$. We can numerically calculate the local value of λ_c after defining $B_\parallel^2 \equiv B_x^2 + B_y^2 - (\boldsymbol{B}\cdot\hat{\boldsymbol{n}}_{\rm rt})^2$, $g_\perp \equiv |\boldsymbol{g}\cdot\hat{\boldsymbol{n}}_{\rm rt}|$, and $\rho_u - \rho_l \equiv |\nabla\rho|\,\Delta L$. Because the perturbation wavelength should be smaller than the scale of the loop-top region, we locate all the positions satisfying $\lambda_c < 0.1$ and find that they show a highly scattered distribution (see the white dots in Figures 3(a1)–(a3)). Moreover, moving with turbulent flows, these isolated positions vary dynamically in time (see the animation of Figure 3), which means that their lifetime might be too short to initiate the RTI.

In contrast, the main shear layers triggering the KHI typically extend $\sim 0.1L_0$ continuously in space. With the development of the KHI, the shapes of the shear layers vary gradually in time but their spatial scales are approximately maintained (see Figure 3). Meanwhile, in our previous simulations in which gravity is not included and the RTI effect is ignorable, the loop-top oscillations can still be observed (see Wang et al. 2021). Therefore, we can conclude that the KHI dominates the symmetry breaking of the loop-top region and thus the initialization of CS oscillations.

3.3. Propagation Properties of CS Oscillations

We further quantitatively analyze the propagation properties of the CS oscillation. Based on the method introduced in the Appendix, we determine the central positions $x_{\rm cs}(y)$ of the CS (see Figures 2(b1)–(b6) and 4(b)). The time–distance plot of the positions clearly shows some wavelike structures (Figure 4(a)). During the first three oscillations, both the amplitude and the period grow (see Figure 4(c)), and the maximum oscillation amplitude reaches $\sim$0.01. Though damping as propagating upward, the oscillation can still be clearly detected at a high altitude (see Figure 4(a)).

To estimate the propagation speed of the perturbations, we take six contours in Figure 4(a) and denote them by $y_p^i(t)$, where $i = 1, 2, ..., 6$ (see Figure 4(a)). These contour lines track the propagation of the perturbations causing a zero-displacement at the x-direction. Note that, the propagation curves contain small noises caused by the motion of magnetic islands. We fit the contour lines by the power function to clean the noises and then take their time derivatives to obtain the propagation speeds, namely, $V_p^i(y)$. The speeds calculated from six different tracks are very similar and we take their averaged value $\langle V_p^i\rangle$ to evaluate their mean feature (see Figure 5(a)). The speed increases from 0.89 to 2.17 with height, corresponding to the real values from 388 to 946 km s^{-1}. Furthermore, we calculate the local Alfvén speed at the CS outer boundary ($V_{\rm Acs}$). It is found that the variations of $\langle V_p^i\rangle$ with height are largely similar to the profile of the time-averaged Alfvén speed $\langle V_{\rm Acs}\rangle$ (see Figure 5(a)).

Considering the similarity between $\langle V_{\rm Acs}\rangle$ and $\langle V_p^i\rangle$, we propose a novel way to determine the magnetic field strength of the CS outer boundary. Observationally, one can use the averaged propagation speeds of several CS oscillations, $\langle V_p^i\rangle$, as a proxy of the local Alfvén speed. With a combination of the plasma density estimated by differential emission measure (DEM), the magnetic field strength of the CS boundary is then derived as

$$\langle B_{\rm Acs}\rangle = \langle V_{\rm Acs}\rangle\sqrt{\langle\rho_{\rm Acs}\rangle} \approx \langle V_p^i\rangle\sqrt{\langle\rho_{\rm Acs}\rangle} = \langle B_p^i\rangle. \tag{4}$$

Here, we verify this method using the numerical data (Figure 5). The time-averaged value $\langle\rho_{\rm cse}\rangle$ is used to simulate the density derived by the DEM analysis (Figures 5(b1) and (b2)). We find that the profiles of $\langle B_p^i\rangle$ we evaluated are basically in agreement with the distribution of $\langle B_{\rm Acs}\rangle$ in height (see Figure 5(c)).

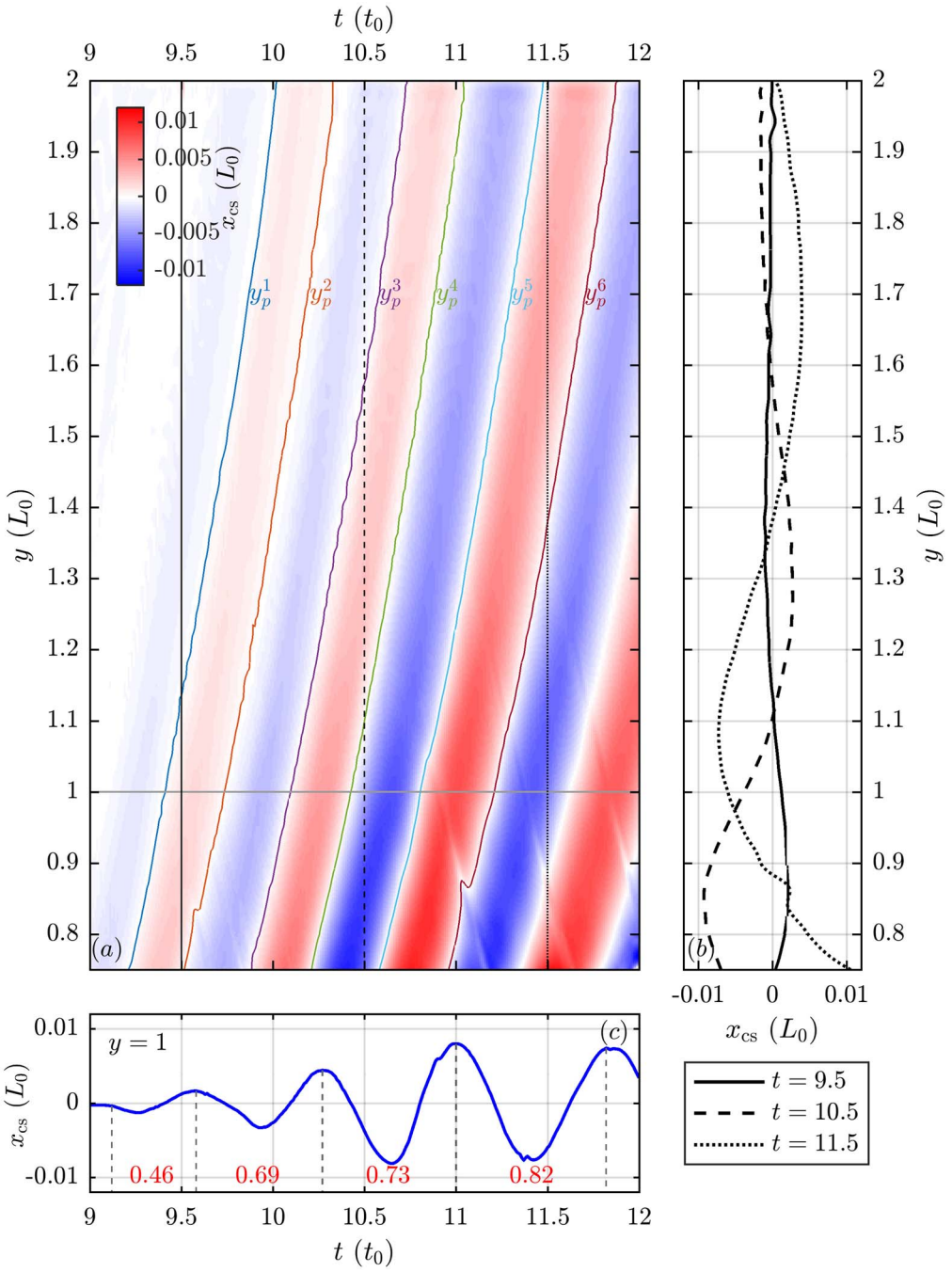

Figure 4. (a) The time–distance plot of the central positions of the CS $x_{cs}(y)$ from $t = 9$ to 12. (b) The profiles of the CS positions x_{cs} at $t = 9.5$, 10.5, and 11.5. (c) The temporal evolution of the CS position x_{cs} at $y = 1$. The red numbers in panel (c) record the periods of four oscillations. The colored curves in panel (a) are six contours of $x_{cs} = 0$. The high-frequency noises in x_{cs} have been filtered. An animation of this figure is available online. The video, with a duration of 19 s, shows the dynamical evolution of $x_{cs}(y)$.

(An animation of this figure is available.)

4. Summary and Discussion

In this letter, we study the formation mechanism of CS oscillations using MHD simulation. The fully developed reconnection presents a quasiperiodic feature. Various downflow magnetic islands collide with the flare loop top and result in a turbulent cusp-shaped structure. Following the collision of a relatively large island at the loop top, fewer and smaller islands are generated. The KHI is then switched on in the interface of two sheared flows from the persistent reconnection downflows. The asymmetric flows, caused by the asymmetric KHI, finally drive large-amplitude swaying of the flare loop top and thus the oscillations of the CS.

CS oscillations, though damping with distance, are still detectable when they propagate to a higher height. More importantly, CS oscillations are proven to propagate with the local Alfvén speed. They thus can be used for evaluating the magnetic field strength of the outer boundary of the CS once we derive the local plasma density, for example, through the DEM technique. This method is well verified by our numerical data and is hopeful to be comparable with other

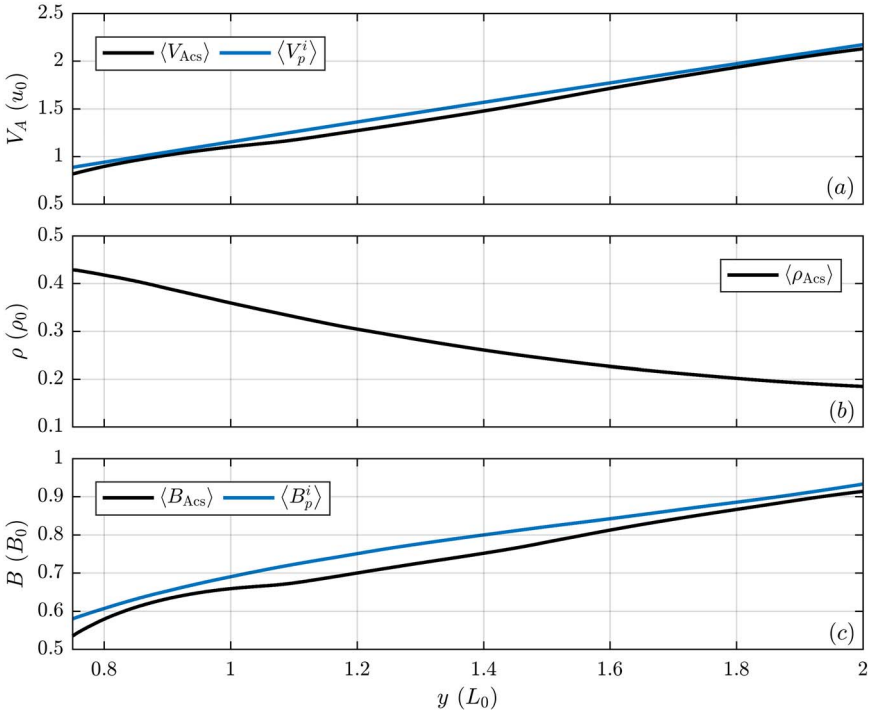

Figure 5. (a) The profiles of time-averaged local Alfvén speed at the CS outer boundary (the black curve) and the averaged propagation speeds of the CS oscillation (the blue curve). (b) The time-averaged density at the CS outer boundary. (c) The distributions of time-averaged magnetic strength at the CS outer boundary (the black curve) and the magnetic field strength evaluated by $\langle B_p^i\rangle = \langle V_p^i\rangle\sqrt{\langle\rho_{\rm Acs}\rangle}$ (the blue curve). The CS outer boundaries are defined by $x = \pm 0.05$ and $y > 0.75$ (see Figure 2(d6)) and $V_{\rm Acs}$, $\rho_{\rm Acs}$, and $B_{\rm Acs}$ are averaged values on both boundaries. $\langle\cdot\rangle$ denotes taking time-average in duration $t \in [9, 12]$.

methods (e.g., Nakariakov & Ofman 2001; Chen et al. 2011; Liu et al. 2011; Tian et al. 2012; Yang et al. 2020). However, note that this method only provides a zero-order approximation of magnetic field strength. Observationally, the main challenge is how to accurately measure the propagation speed of CS oscillations, which are largely limited by observational tempo-spatial resolution. Our result shows that the magnetic field at the outer boundary of the CS increases with the height, which is different from real observations and recent simulations of the flux rope eruption that use decaying magnetic fields in height (e.g., Chen et al. 2020). The main reason is that we take advantage of a uniform background magnetic field along the y-direction and the appearance of upward moving magnetic islands during the CS oscillations.

Differing from Takahashi et al. (2017), in which the oscillations above the flare loops were also reproduced but for the TS fronts, here, we mainly focus on the fundamental mechanism and properties of large-amplitude oscillations of the whole CS. The mechanism for the CS oscillations revealed here is different from that in Xie et al. (2021) who considered the effects of CMEs but did not include thermal conduction, radiation cooling, and background heating. They contributed the CS oscillations to the RTI at the bottom of a CME. Although excluding the flux rope eruption, our model provides much more fine structures at the loop-top region. We find that, the positions where the RTI may be initiated are spatially scattered and temporally varied and thus, compared with the RTI, the KHI plays a more important role in giving rise to CS oscillations.

We would like to thank the anonymous referee for valuable suggestions. This research is supported by the Natural Science Foundation of China grants 11722325, 11733003, 11790303, and 11790300.

Appendix
The CS Structure

We take four typical slits across the CS at $t = 9.1$ to exhibit the detailed CS structures (see Figure A1(e)). The red dashed lines mark the position with the maximum temperature gradients ($|\partial T/\partial x|$) on both sides of the CS, which approximately correspond to the discontinuity fronts of the slow-mode shocks (also see Mei et al. 2012). We take their average x-coordinate as the central position $x_{\rm cs}(y)$ of the CS (see the blue dashed lines in Figure A1).

Between the slow shocks, the polarity of magnetic field reverses rapidly in space (see Figures A1(d1)–(d4)). However, differing from standard CS models (e.g., the Harris-sheet or the Petschek-sheet), the CS structure shows complex details. Near the principal X-point ($y = 1.1$), the CS is thinnest and shows a Gauss-type distribution. At $y = 0.8$ and $y = 1.8$, on both sides of the CS, the slow-shock fronts cause rapid decreases of magnetic field strength and thus induce two localized strong currents, between which a lower current plateau forms. J_z near $x = 0$ can be either negative (Figure A1(c1), also see Mei et al. 2012) or positive (Figure A1(c4)). Near the center of a magnetic island ($y = 1.356$), the density and current increase significantly (Figures A1(a3) and (c3)), while the temperature and magnetic field profiles are similar with other slits (Figures A1(b3) and (d3)).

For all four positions, however, one can see that the region of the CS is well enclosed by the red dashed lines and is approximately symmetric about the blue dashed lines. Therefore, we determine the central position of the CS by the blue dashed line.

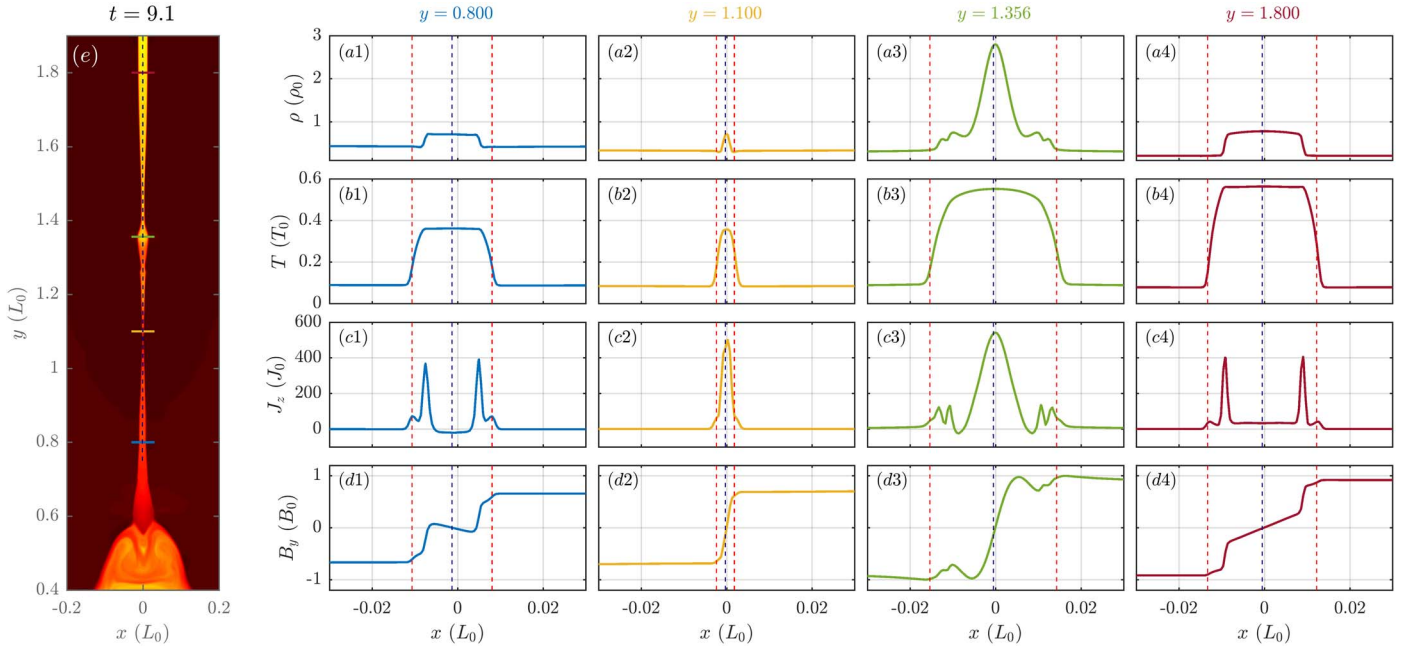

Figure A1. The CS structure at $t = 9.1$. (e) The temperature distribution of the CS at $t = 9.1$ (also see Figure 2(b1)). The blue, yellow, green, and brown slits are taken at $y = 0.8$, 1.1, 1.356, and 1.8 across the CS, respectively. (a1), (b1), (c1), and (d1) are, respectively, the profiles of ρ, T, J_z, and B_y along the blue slit at $y = 0.8$. (a2)–(d2), (a3)–(d3), and (a4)–(d4) are the same as (a1)–(d1) but for different slits. The red dashed lines mark the positions with the maximum temperature gradient ($|\partial T/\partial x|$) on both sides of the CS, while the blue dashed lines denote the average positions of the red ones.

ORCID iDs

Yulei Wang https://orcid.org/0000-0001-9863-5917
Xin Cheng https://orcid.org/0000-0003-2837-7136
Mingde Ding https://orcid.org/0000-0002-4978-4972

References

Bhattacharjee, A., Huang, Y.-M., Yang, H., & Rogers, B. 2009, PhPl, 16, 112102
Cai, Q., Shen, C., Raymond, J. C., et al. 2019, MNRAS, 489, 3183
Carlyle, J., & Hillier, A. 2017, A&A, 605, A101
Carmichael, H. 1964, in Proc. of the AAS-NASA Symp. 50, The Physics of Solar Flares, ed. N. Hess. Wilmot (Washington, DC: NASA), 451
Chen, B., Shen, C., Gary, D. E., et al. 2020, NatAs, 4, 1140
Chen, Y., Feng, S. W., Li, B., et al. 2011, ApJ, 728, 147
Chen, Y., Song, H. Q., Li, B., et al. 2010, ApJ, 714, 644
Cheng, X., Li, Y., Wan, L. F., et al. 2018, ApJ, 866, 64
Ciaravella, A., Raymond, J. C., Li, J., et al. 2002, ApJ, 575, 1116
Hillier, A. S. 2016, MNRAS, 462, 2256
Hirayama, T. 1974, SoPh, 34, 323
Jones, T. W., Gaalaas, J. B., Ryu, D., & Frank, A. 1997, ApJ, 482, 230
Klimchuk, J. A., Patsourakos, S., & Cargill, P. J. 2008, ApJ, 682, 1351
Ko, Y., Raymond, J. C., Lin, J., et al. 2003, ApJ, 594, 1068
Kong, X., Guo, F., Shen, C., et al. 2020, ApJL, 905, L16
Kopp, R. A., & Pneuman, G. W. 1976, SoPh, 50, 85
Lee, J.-O., Cho, K.-S., Nakariakov Valery, M., et al. 2021, JKAS, 54, 61
Lemen, J. R., Title, A. M., Akin, D. J., et al. 2012, SoPh, 275, 17
Li, L. P., Zhang, J., Su, J. T., & Liu, Y. 2016, ApJL, 829, L33
Lin, J., & Forbes, T. G. 2000, JGRA, 105, 2375
Lin, J., Murphy, N. A., Shen, C., et al. 2015, SSRv, 194, 237
Ling, A. G., Webb, D. F., Burkepile, J. T., & Cliver, E. W. 2014, ApJ, 784, 91
Liu, R., Lee, J., Wang, T., et al. 2010, ApJL, 723, L28
Liu, W., Title, A. M., Zhao, J., et al. 2011, ApJL, 736, L13
McKenzie, D. E. 2013, ApJ, 766, 39
Mei, Z., Shen, C., Wu, N., et al. 2012, MNRAS, 425, 2824
Meyer, C. D., Balsara, D. S., & Aslam, T. D. 2014, JCoPh, 257, 594
Miyoshi, T., & Kusano, K. 2005, JCoPh, 208, 315
Nakariakov, V. M., & Ofman, L. 2001, A&A, 372, L53
Ni, L., Lin, J., Roussev, I. I., & Schmieder, B. 2016, ApJ, 832, 195
Patsourakos, S., & Vourlidas, A. 2011, A&A, 525, A27
Pesnell, W. D., Thompson, B. J., & Chamberlin, P. C. 2012, SoPh, 275, 3
Ryu, D., Jones, T. W., & Frank, A. 2000, ApJ, 545, 475
Samanta, T., Tian, H., & Nakariakov, V. M. 2019, PhRvL, 123, 035102
Shen, C., Chen, B., Reeves, K. K., et al. 2022, NatAs, 6, 317
Shen, C., Kong, X., Guo, F., Raymond, J. C., & Chen, B. 2018, ApJ, 869, 116
Shen, C., Lin, J., & Murphy, N. A. 2011, ApJ, 737, 14
Shibata, K., Masuda, S., Shimojo, M., et al. 1995, ApJL, 451, L83
Stone, J. M., Tomida, K., White, C. J., & Felker, K. G. 2020, ApJS, 249, 4
Sturrock, P. A. 1966, Natur, 211, 695
Takahashi, T., Qiu, J., & Shibata, K. 2017, ApJ, 848, 102
Takasao, S., Matsumoto, T., Nakamura, N., & Shibata, K. 2015, ApJ, 805, 135
Takasao, S., & Shibata, K. 2016, ApJ, 823, 150
Tian, H., McIntosh, S. W., Wang, T., et al. 2012, ApJ, 759, 144
Verwichte, E., Nakariakov, V. M., & Cooper, F. C. 2005, A&A, 430, L65
Wang, Y., Cheng, X., Ding, M., & Lu, Q. 2021, ApJ, 923, 227
Webb, D. F., Burkepile, J., Forbes, T. G., & Riley, P. 2003, JGRA, 108, 1440
Xie, X., Mei, Z., Huang, M., et al. 2019, MNRAS, 490, 2918
Xie, X., Mei, Z., Shen, C., et al. 2021, MNRAS, 509, 406
Yang, Z., Bethge, C., Tian, H., et al. 2020, Sci, 369, 694
Ye, J., Cai, Q., Shen, C., et al. 2020, ApJ, 897, 64
Ye, J., Shen, C., Raymond, J. C., Lin, J., & Ziegler, U. 2019, MNRAS, 482, 588
Yokoyama, T., & Shibata, K. 2001, ApJ, 549, 1160
Zhao, X., & Keppens, R. 2020, ApJ, 898, 90